Published in final edited form as:
IEEE Trans Nucl Sci. 2010 June 1; 57(3): 1038–1044. doi:10.1109/TNS.2010.2046753.

Performance Characteristics of BGO Detectors for a Low Cost Preclinical PET Scanner

H. Zhang[Member, IEEE],
UCLA David Geffen School of Medicine, Crump Institute for Molecular Imaging, Los Angeles, CA 90095 USA, on leave from the Department of Biomedical Engineering, Tsinghua University, Beijing 100084, China

N. T. Vu[Member, IEEE],
UCLA David Geffen School of Medicine, Crump Institute for Molecular Imaging, Los Angeles, CA 90095 USA

Q. Bao,
UCLA David Geffen School of Medicine, Crump Institute for Molecular Imaging, Los Angeles, CA 90095 USA

R. W. Silverman[Senior Member, IEEE],
UCLA David Geffen School of Medicine, Crump Institute for Molecular Imaging, Los Angeles, CA 90095 USA

B. N. Berry-Pusey,
UCLA David Geffen School of Medicine, Crump Institute for Molecular Imaging, Los Angeles, CA 90095 USA

A. Douraghy,
UCLA David Geffen School of Medicine, Crump Institute for Molecular Imaging, Los Angeles, CA 90095 USA

D. A. Williams,
UCLA David Geffen School of Medicine, Crump Institute for Molecular Imaging, Los Angeles, CA 90095 USA

F. R. Rannou,
Departmento de Ingenieria Informatica, Universidad de Santiago de Chile (USACH), Chile

D. B. Stout[Member, IEEE], and
UCLA David Geffen School of Medicine, Crump Institute for Molecular Imaging, Los Angeles, CA 90095 USA

A. F. Chatziioannou[Senior Member, IEEE]
UCLA David Geffen School of Medicine, Crump Institute for Molecular Imaging, Los Angeles, CA 90095 USA

H. Zhang: huizhang@mednet.ucla.edu; F. R. Rannou: fernando.rannou@usach.cl; A. F. Chatziioannou: archatziioann@mednet.ucla.edu

Abstract

PETbox is a low-cost benchtop PET scanner dedicated to high throughput preclinical imaging that is currently under development at our institute. This paper presents the design and characterization of the detectors that are used in the PETbox system. In this work, bismuth germanate scintillator

Color versions of one or more of the figures in this paper are available online at http://ieeexplore.ieee.org.

was used for the detector, taking advantage of its high stopping power, high photoelectric event fraction, lack of intrinsic background radiation and low cost. The detector block was segmented into a pixelated array consisting of 20 × 44 elements, with a crystal pitch of 2.2 mm and a crystal cross section of 2 mm × 2 mm. The effective area of the array was 44 mm × 96.8 mm. The array was coupled to two Hamamatsu H8500 position sensitive photomultiplier tubes, forming a flat-panel type detector head with a sensitive area large enough to cover the whole body of a typical laboratory mouse. Two such detector heads were constructed and their performance was characterized. For one detector head, the energy resolution ranged from 16.1% to 38.5% full width at half maximum (FWHM), with a mean of 20.1%; for the other detector head, the energy resolution ranged from 15.5% to 42.7% FWHM, with a mean of 19.6%. The intrinsic spatial resolution was measured to range from 1.55 mm to 2.39 mm FWHM along the detector short axis and from 1.48 mm to 2.33 mm FWHM along the detector long axis, with an average of 1.78 mm. Coincidence timing resolution for the detector pair was measured to be 4.1 ns FWHM. These measurement results show that the detectors are suitable for our specific application.

Index Terms

Bismuth germanate (BGO) scintillator; detector; positron emission tomography (PET); small animal imaging

I. Introduction

Small animal positron emission tomography (PET) has been successfully used in preclinical research over the past decade. A number of research groups have been actively involved in the development of dedicated PET scanners for small animal imaging [1]–[9], with most efforts focused on improving system performance in terms of spatial resolution and sensitivity [10]. Issues of scanner cost versus system performance and complexity have also been addressed in [11]–[14] by using partial ring or double head geometries. Considering the rapid growth in the number of small animal imaging studies, there is still a lack of a range of solutions to accommodate the diversity of preclinical imaging studies that are performed with PET. We believe that a low cost benchtop PET scanner dedicated to high throughput pharmacokinetic and pharmacodynamic studies is of significant interest in preclinical research. The development of such a system, namely PETbox, is currently underway at our institute.

PETbox is designed as a low cost, easy to use, benchtop PET scanner optimized for imaging mice. The system is mainly targeted for dedicated screening studies such as biodistribution and organ uptake quantification. Fig. 1 shows a simplified conceptual drawing of the PETbox geometry. This geometry is similar to those of positron emission mammography (PEM) systems [15] or a PET/planar small animal imaging system [13] and a high-sensitivity small-animal PET system based on High-Resolution Research Tomograph (HRRT) detector technology [16]. The system incorporates two flat-panel type detector heads placed opposing each other at a small spacing. The detectors and the imaging subject (mouse) are kept stationary during the scan, providing a limited angle tomography along the central anterior-posterior (AP) view. Each detector has a sensitive area of approximately 5 cm × 10 cm, and the separation between them is 5 cm, providing both a large detection solid angle (~ 43.6%) and a sensitive volume large enough to cover a typical laboratory mouse (20–35 g). An iterative reconstruction method based on a maximum likelihood and expectation maximization (ML-EM) algorithm with the incorporation of a system probability matrix (P-matrix) has been developed to reconstruct 3D images from the limited angle projection data [17].

Monte Carlo simulations have been performed for the PETbox scanner to provide quantitative analysis of system performance and guide decisions on major system parameters [18]. Based on the simulation results, a prototype system has been developed. This paper describes the design and development of the detectors for the PETbox scanner. Evaluations were conducted to characterize the performance of the detectors and the results are reported.

II. Materials and Methods

A. The Scintillator Material

For the choice of the scintillator material, the following characteristics were considered and evaluated: (a) stopping power, (b) cost and availability, (c) timing performance, (d) light output, (e) intrinsic background and (f) ease of handling. In recent years, lutetium oxyorthosilicate (LSO) and its variants have become a popular choice of scintillator in many investigations for pre-clinical PET [1]–[3], [6], [19]–[21]. The two major advantages of LSO crystals are the high light output which generally improves spatial resolution, and fast decay time which leads to a better count rate performance. In this work, however, bismuth germanate (BGO) scintillator was chosen to construct the PETbox detectors. BGO is one of the earliest scintillation materials that have been used in PET tomographs. It is also one of the lower cost scintillators. BGO is mechanically strong, rugged and non-hygroscopic and can be easily cut and polished with established methods [22]. BGO has a high effective atomic number (Z) which increases the probability of a photoelectric event at the first interaction site. This helps to reduce inter-crystal scatter, which becomes significant as the individual crystal size is reduced to achieve higher spatial resolution. BGO also has very high stopping power for 511 keV photons comparable to that of LSO and therefore requires little material thickness to provide adequate system sensitivity. This is important for the close detector/gantry geometry we chose for the PETbox in which scintillator thickness will cause significant resolution loss due to parallax errors. BGO has very low intrinsic radioactivity [23], which is about 35 times lower than that of LSO. Considering the very compact geometry of PETbox, high intrinsic radioactivity from a large volume of crystals such as LSO could adversely affect the system minimum detectable activity [24], [25].

It has been shown that during preclinical PET imaging procedures with a typical amount of activity of 7.4 MBq (200 μCi) administered, the major organs and tumor xenografts of mice could receive an absorbed dose in a range for which biological effects have been reported [26], [27]. It is therefore desirable to reduce the dose delivered to mice, especially in the case of longitudinal studies, in which multiple experiments take place. For typical biodistribution studies that will be performed with PETbox, we anticipate to reduce the dose by a factor of 4, which corresponds to an injected activity of 1.85 MBq (50 μCi). Although BGO is a relatively slow scintillator with a decay time of 300 ns, it can provide adequate count rate performance at this low activity level. Another drawback of BGO is the lower light output compared with lutetium based scintillators. However, our preliminary experiments showed that we were able to resolve 5 mm thick BGO arrays with pixel sizes down to 2 mm, which suggests that BGO provides adequate performance for the PETbox system considering the main performance metrics we expect. The simulation results in [18] also validated the choice of BGO over other scintillators for the PETbox scanner.

B. Detector Module Design

To construct the detector, we use the Hamamatsu H8500 position sensitive photomultiplier tube (PSPMT) (Hamamatsu Photonics, Bridgewater, NJ) because of its large effective area (49 mm × 49 mm) and high overall packing fraction. Fig. 2(a) shows the schematic drawing of the detector module. The BGO array is coupled to two H8500 tubes to form a detector

with an effective area of approximately 5 cm × 10 cm. A problem with this configuration is that a dead space of approximately 3.5 mm is present at the junction of the two PSPMTs. This dead space is caused by the casing of the PSPMT as well as a gap between the two tubes due to manufacturer's mechanical tolerances. To overcome this problem, a 2 mm thick glass layer was inserted between the scintillator array and the PSPMTs to act as a light guide and enable light sharing between the two PSPMTs above the dead space [21].

The individual crystal size was also carefully evaluated during the detector design. The thickness of the crystal affects system sensitivity significantly. At the same time, as crystal thickness increases, the spatial resolution of the system degrades because of crystal penetration. Based on simulation studies in [18], a thickness of 5 mm was chosen for the BGO scintillator which provided a good compromise between sensitivity and resolution degradation because of oblique angle crystal penetration. The cross section size of each crystal element determines the intrinsic detector resolution. However, if the crystal is too small, inter-crystal scattering will lower event positioning accuracy. Also it would be more difficult to decode individual crystals as they get smaller because of the limited light output of BGO scintillators. Based on our preliminary experiments as well as simulations [18], the crystal cross section size was chosen as 2 mm × 2 mm for the current PETbox system.

C. Detector Module Fabrication

Slabs of raw BGO scintillator measuring 47.2 mm × 100 mm × 5 mm (Proteus Inc., Chagrin Falls, OH) were used to fabricate the scintillator array. Conventionally scintillator arrays are assembled by first cutting the crystal into small individual pieces and then bundled or glued together to form an array [1], [19], [28]. Most small animal PET systems employ individual crystal elements with dimensions on the order of millimeters making the individual crystals difficult to manufacture and handle. In this work, a simple method was used to construct the array. A 2 mm thick borosilicate glass substrate which serves as the light guide was first glued to the raw BGO slab using optical adhesive to form a single block. The block was then cut on the BGO side using an Ultraslice high-precision saw (Ultra Tec, Santa Ana, CA) and segmented into an array of 20 × 44 elements. Fig. 2(b) shows one of the BGO arrays fabricated using the proposed method. The crystal pitch is 2.2 mm and each crystal element measures 2 mm × 2 mm in cross section. The effective area of the resulting array is 44 mm × 96.8 mm. A protective outer perimeter of 1.6 mm material was left around the four edges, which helps to maintain the integrity of the array during successive handling. The raw BGO slabs were grounded on all sides, and no further surface treatment was applied after the cutting. Four pieces of 3M Vikuiti specular reflector (3M Optical Systems, St Paul, MN) were inserted into the grooves between the edge crystals and the inner crystals to improve the identification of edge crystals. However no reflectors were used elsewhere in the array to simplify the fabrication process. Teflon tape was used to cover the BGO top surface while all other sides were wrapped with black tape for the finished array.

The BGO array is coupled to a pair of H8500 PSPMTs as shown in the schematic in Fig. 2(a). Optical grease (BC-630; Saint-Gobain, Valley Forge, PA) was used for the coupling between the glass substrate of the array and the PSPMTs. The detector module is encased in an aluminum bracket measuring 101.6 mm × 152.4 mm × 101.6 mm which provides a light tight housing for the detector module. A shallow pocket structure was designed on the front plate of each bracket to hold the BGO array in place. An aluminum frame was built to mount the two opposing detector heads, with the front surfaces of the two BGO arrays separated by 5 cm. A photograph of the gantry with the two detector heads assembled is shown in Fig. 2(c).

D. Detector Module Multiplexed Readout

The two PSPMTs in each detector head are read out using a charge division resistor network [29] which converts the 128 anode outputs from the two PSPMTs into four corner signals. The four corner signals are further reduced to two position encoding signals, denoted as *x* and *y*, and the sum of the four corner signals, denoted as *sum*. Event locations are determined based on Anger logic and coordinates are calculated as $X = x/sum$ and $Y = y/sum$. The H8500 PSPMT allows direct connection to the 12th dynode signal which can be used to generate event timing triggers. The last dynode signals from the two PSPMTs are summed together and amplified to provide the timing signal.

E. The Data Acquisition Unit

Field programmable gate array (FPGA) based systems have recently been adopted to replace conventional analog circuitry in some small animal PET systems [30]–[33]. An FPGA based digital signal processing board (VHS-ADC V4; Lyrtech, Quebec, Canada) was used in this work for data acquisition and signal processing. Position and timing signals from the two detectors are connected to the 8 input channels on the VHS-ADC V4 board, where they are digitized using eight 100 MHz free-running analog-to-digital converters. The digital samples are sent to a Virtex-4 FPGA device (Xinlinx, San Jose, CA) and processed using custom developed event detection algorithms. Singles and coincidence events from the two detectors are sorted in the FPGA and saved to hard disk as list-mode data files, which can be accessed by a host PC for further processing.

F. Detector Performance Characterization

Two detector heads were assembled and their performance was characterized. The two detectors are referred to as the top detector and bottom detector in Section III as indicated by their relative positions in Fig. 2(c).

1. *Flood Histograms:* Flood histograms were taken for the two detector heads using a 0.185 MBq ^{68}Ge(5 μCi) uniform planar source (Isotope Products Laboratories, Valencia, CA) with a size of 60 mm × 110 mm and a thickness of 3 mm. The source was placed midway between the detectors. The FPGA-based data acquisition unit was configured to record singles from both detector heads simultaneously. The event detection threshold was set to just above the electronic noise. The recorded list mode data file was sorted into two dimensional detector flood histograms. Boundaries of the crystal elements in the flood histograms were determined using a semi-automated program and crystal look-up tables (LUT) were generated accordingly. A 1 hour acquisition was performed with approximately 60 million events recorded for each detector head.

2. *Energy Histograms:* The energy deposited by an event was measured as the integration of the *sum* signal from the readout circuitry. Event energy was recorded to the list mode data file while acquiring the flood histograms. Energy spectra of individual crystals were extracted using crystal LUTs generated in the previous section. A Gaussian function was fitted to the energy spectra and the energy resolution was measured as the full width at half-maximum (FWHM) of the Gaussian function divided by the energy (511 keV photopeak).

3. *Coincidence Timing Resolution:* For coincidence timing measurements, a 0.74 MBq ^{68}Go(20 μCi) point-like source (Isotope Products Laboratories, Valencia, CA) was positioned midway between the detectors. The FPGA-based data acquisition unit was configured to detect coincidence events from the two detector heads with a coincidence timing window of 30 ns and an open global energy window. The difference in the arrival time between a pair of coincidence events was recorded to

the list mode data file. Singles count rates from both detectors were observed to ensure that random coincidences were negligible. The recorded coincidence time was histogrammed and fitted with a Gaussian function. The FWHM of the fitted plot provids a measure of the coincidence timing resolution between the two detector heads.

4. *Intrinsic Spatial Resolution:* The intrinsic spatial resolution was measured using a 0.75 MBq ^{22}Na(20.2 μCi) point source with a nominal size of 0.3 mm, embedded in a acrylic plastic disk measuring 25 mm in diameter and 5 mm in height (Isotope Products Laboratories, Valencia, CA). The source was attached to a translation stage and placed midway between the two detectors. Starting from the center of the field of view (FOV), the source was stepped across the face of the detector, first along the detector short axis and then along the detector long axis. A step size of 0.4 mm was used for both directions. An assumption was made that the detector pair configuration is symmetric and therefore measurements were performed along only half of the detector FOV in both directions. The FPGA-based data acquisition unit was configured to run in coincidence mode and the acquisition time was 90 seconds for each measurement position. The recorded data were processed to determine the number of coincidence counts between directly opposing crystal pairs from the two detectors. The count distribution of each crystal pair was plotted as function of the source location. The plot was fitted with a Gaussian function and the FWHM was calculated to determine the intrinsic spatial resolution of the detectors.

G. Initial Imaging Study

A prototype PETbox system has been built using the proposed detectors. An initial imaging study was performed with a mouse tumor xenograft. The mouse was injected with 32 μCi of [^{18}F]FDG and following a 1 hour uptake period it was scanned for 20 minutes. The coincidence timing window was set to 30 ns and list mode data were acquired with an open global energy window. The list mode data were then histogrammed into a sinogram, during which an energy window of 150–650 keV was applied. 3D images were reconstructed using the iterative ML-EM method presented in [17]. Typical image matrix size was 80 × 80 × 176 with voxel dimensions of 0.55 mm × 0.55 mm × 0.55 mm.

III. Results

A. Flood Histograms

Fig. 3(a) shows the flood histogram taken for the top detector. In the flood histograms from both detectors, most of the crystal elements in the 20 × 44 BGO array are clearly identified, except for a few corner crystals which require manual estimation and adjustment of borders. Crystals sitting on top of the junction of the two PSPMTs have fewer counts due to poorer light collection. However they can be clearly identified, indicating that the dead space is successfully recovered by using the light guide. The introduction of reflectors between the edge crystals and the inner crystals helps the separation and identification of the edge crystals, which is evident in Fig. 3(a). Profiles across the flood histograms are taken and peak-to-valley ratios are examined to provide a quantitative measure of crystal separation. Fig. 3(b) and (c) show two profiles along the 17th column and 10th row in the top detector flood histogram. Due to a combination of inter-crystal scatter, light spread in the light guide and optical crosstalk between crystals, the measured peak-to-valley ratios are poor, with an average value of approximately 1.9 along the column direction and 1.5 along the row direction. Nonetheless, the boundaries of individual crystals could be drawn without difficulty for both detectors.

It is worthwhile to note that the arrays were fabricated with a protective outer perimeter of crystals, which can be partially seen in the flood histograms. Although they are discarded in the generated LUT, events from these crystals cannot be excluded completely due to the difficulties in drawing accurate borders between the outer perimeter of crystals and the edge crystals. Subsequent evaluation of the crystal blocks showed that the mechanical integrity of the arrays was not problematic provided careful handling was used. This outer perimeter of crystals will be removed from the arrays in future designs.

B. Energy Resolution

Table I lists the measured energy resolution for the two detector heads. The average energy resolution is approximately 20% for both detectors. The 511 keV energy amplitude (511 keV photopeak position in the energy spectra) for each individual crystal was also determined. The ratio between the maximum and minimum amplitude was measured to be 3.4:1 and 3.5:1 for the two detectors respectively, indicating large variations between individual crystals, which are believed to be caused by the crystal-to-crystal difference in terms of light collection and PSPMT detection efficiency. Fig. 4 shows the energy spectra of four individual crystals on the top detector. It was observed that crystals at the center of each PSPMT tend to yield better energy resolution than edge crystals or crystals at the junction of the two PSPMTs.

C. Coincidence Timing Resolution

The coincidence timing histogram of the detector pair is shown in Fig. 5. Gaussian curve fitting was applied to the plot, and the coincidence timing resolution was measured to be 4.1 ns FWHM. However, strong tails were observed in the distribution. While the data shown in Fig. 5 were acquired with an open global energy window, a narrow energy window can be applied in post-processing, which will cut the tails to some extent. But tails are still evident even at a 350–650 keV energy window, suggesting that other sources contribute to the tails besides low energy events. This result requires further investigation to identify these sources.

D. Intrinsic Spatial Resolution

The intrinsic spatial resolution of the detector pair is shown in Fig. 6. The FWHM was calculated for the profiles of the 10 crystal pairs along the detector short axis and the 22 crystal pairs along the detector long axis. The average FWHM was measured to be 1.78 mm. For crystal pairs along the detector short axis, the measured FWHM ranged from 1.55 mm to 2.39 mm, with an average value of 1.84 mm. For crystal pairs along the detector long axis, the measured FWHM ranged from 1.48 mm to 2.33 mm, with an average value of 1.72 mm.

E. Initial Imaging Studies

Fig. 7 shows the reconstructed images from the initial imaging study. No attenuation, scatter or normalization correction was applied in this study. Random coincidences were corrected using a delayed window subtraction method. Two slices of a coronal section of the mouse are shown in Fig. 7. The slice thickness is 0.55 mm. On the left image the heart uptake can be clearly identified while on the right image the tumor accumulation can be clearly identified, including a large tumor necrotic center.

IV. Discussion and Conclusion

In the work presented here, a crystal cross section size of 2 mm × 2 mm was chosen. The measured intrinsic spatial resolution is similar to those reported for other BGO based systems [15], [22], and it is believed to be sufficient for biodistribution measurements in

most of the major organs, matching the main target of the proposed PETbox scanner. While our initial efforts were focused on proof of concept, optimization of the scintillator array was not pursued. However, several improvements can be readily made including crystal polishing and reflective material packing between crystal elements [22]. In principle, the crystals can be cut smaller in cross section to achieve a better intrinsic spatial resolution. But there are other factors that also need to be taken into consideration when determining the crystal size, including inter-crystal scattering which will lower event positioning accuracy, light output from the individual crystal which will limit crystal identification, and material loss due to the cutting which will lead to system sensitivity loss.

The two H8500 PSPMTs used for each PETbox detector module have different specified gains. In order to balance the signal gain between the two tubes, the high voltage for each tube was individually adjusted until the total counts from the two PMT areas were approximately the same in the acquired flood histogram. Nonetheless, the non-uniformity between a total of 128 anodes on the two tubes, together with other factors such as light collection efficiency, lead to significant variation in the overall detection efficiency from crystal to crystal. This is evident in the measured energy resolutions as well as in the coincidence timing distribution. There are several implications for applications of these detectors. First, an open global energy window needs to be employed in hardware to accept events from areas with poorer efficiency. An energy window for each crystal can be applied later for event discrimination. Secondly, a fairly large coincidence timing window (≥ 20 ns) should be used. Normally, the cost of using a large timing window is increased random events collected by the system. However, the PETbox system is intended to be used with small amounts of injected activity, so this issue has reduced significance. Our simulations show that the random rate would be very low, at a percentage of ~ 2% of the total coincidence events with a 20 ns timing window and a 50 μCi activity injection [18]. Lastly, the non-uniformity presented between crystals needs to be addressed in the normalization step of post processing algorithms to yield quantitatively meaningful results. For the prototype system built in our lab with the presented detectors, a full system optimization was performed regarding these issues and will be presented elsewhere.

The PETbox system was designed for use with low levels of administered dose. This is achieved by employing a compact system geometry optimized for imaging mice as well as by using a scintillator which has a very low intrinsic radioactivity. Our simulation shows that the absolute sensitivity at the center of FOV is 3.87% with a 150–650 keV energy window. The initial imaging study shown in this manuscript also demonstrates the utility of the system at low activity levels. Despite the fact that a limited-view reconstruction is used for the PETbox system, initial results in [17] show reasonably good quantification accuracy for most large organs, mainly limited by the system spatial resolution. That is in line with a previous report in [34], where a dual headed system incorporating a full system response provided accurate quantitative results. A full investigation of the quantification capabilities of the PETbox system is still underway.

Finally, it is important to emphasize that the goal of the proposed PETbox system is for high throughput preclinical pharmacokinetic and pharmacodynamic mouse studies. To simplify the development and increase the robustness of the system, conventional and proven detector technologies were adopted lowering the cost. The performance of the detectors was optimized for mouse imaging applications. Very high performance detectors were not among the goals of the work presented in this manuscript, but the proposed detector showed satisfactory results for the specific applications. A prototype PETbox system has been built and more detailed system performance evaluations as well as mouse imaging studies are currently underway.

Acknowledgments

This work was supported in part by National Institutes of Health under Grant R24 CA92865 and by the Department of Energy under Contract DE-FC03-02ER63420. The work of F. R. Rannou was supported by FONDECYT Grant 1080465 Chile.

The authors would like to thank D. A. Williams for helping them build the detector brackets and gantry. They would also like to thank R. Taschereau for his assistance and valuable discussions.

References

1. Cherry SR, Shao Y, Silverman RW, Meadors K, Siegel S, Chatziioannou AF, Young JW, Jones W, Moyers JC, Newport D, Boutefnouchet A, Farquhar TH, Andreaco M, Paulus MJ, Binkley DM, Nutt R, Phelps ME. MicroPET: A high resolution PET scanner for imaging small animals. IEEE Trans Nucl Sci Jun;1997 44(3):1161–1166.
2. Wienhard K, Schmand M, Casey ME, Baker K, Bao J, Eriksson L, Jones WF, Knoess C, Lenox M, Lercher M, Luk P, Michel C, Reed JH, Richerzhagen N, Treffert J, Vollmar S, Young JW, Heiss WD, Nutt R. The ECAT HRRT: Performance and first clinical application of the new high resolution research tomograph. IEEE Trans Nucl Sci Feb;2002 49(1):104–110.
3. Tai YC, Chatziioannou AF, Yang Y, Silverman RW, Meadors K, Siegel S, Newport DF, Stickel JR, Cherry SR. MicroPET II: Design, development and initial performance of an improved microPET scanner for small-animal imaging. Phys Med Biol 2003;48:1519–1537. [PubMed: 12817935]
4. Seidel J, Vaquero JJ, Green MV. Resolution uniformity and sensitivity of the NIH ATLAS small animal PET scanner: Comparison to simulated LSO scanners without depth-of-interaction capability. IEEE Trans Nucl Sci Oct;2003 50(5):1347–1350.
5. Surti S, Karp JS, Perkins AE, Freifelder R, Muehllehner G. Design evaluation of A-PET: A high sensitivity animal PET camera. IEEE Trans Nucl Sci Oct;2003 50(5):1357–1363.
6. Correia JA, Burnham CA, Kaufman D, Brownell AL, Fischman AJ. Performance evaluation of MMP-II: A second-generation small animal PET. IEEE Trans Nucl Sci Feb;2004 51(1):21–26.
7. Miyaoka RS, Janes ML, Lee K, Park BK, Kinahan PE, Lewellen TK. Development of a single detector ring micro crystal element scanner (MiCES): QuickPET II. Mol Imag 2005;4:117–127.
8. Ziemons K, Auffray E, Barbier R, Brandenburg G, Bruyndonckx P, Choi Y, Christ D, Costes N, Declais Y, Devroede O, Dujardin C, Fedorovd A, Heinrichs U, Korjik M, Krieguer M, Kuntner C, Largeron G, Lartizien C, Larue H, Lecoq P, Leonard S, Marteau J, Morel C, Mosset JB, Parl C, Pedrini C, Petrosyan AG, Pietrzyk U, Rey M, Saladino S, Sappey-Marinier D, Simon L, Streun M, Tavernier S, Vieira JM. The ClearPET(TM) project: Development of a 2nd generation high-performance small animal PET scanner. Nucl Instrum Methods Phys Res A 2005;537:307–311.
9. Bergeron M, Cadorette J, Beaudoin JF, Lepage MD, Robert G, Selivanov V, Tetrault MA, Viscogliosi N, Norenberg JP, Fontaine R, Lecomte R. Performance evaluation of the LabPET APD-based digital PET scanner. IEEE Trans Nucl Sci Feb;2009 56(1):10–16.
10. Stickel JR, Cherry SR. High-resolution PET detector design: Modelling components of intrinsic spatial resolution. Phys Med Biol 2005;50:179–195. [PubMed: 15742938]
11. Del Guerra A, Di Domenico G, Scandola M, Zavattini G. YAPPET: First results of a small animal positron emission tomograph based on YAP:Ce finger crystals. IEEE Trans Nucl Sci Dec;1998 45(6):3105–3108.
12. Thompson, CJ.; Sciascia, P.; Murthy, K.; Kecani, S.; Nikkinen, I.; Del Campo, E.; Corbett, JF.; Bercier, Y.; Diksic, M.; Cumming, P. ANIPET: A versatile PET scanner for imaging small animals. Proc IEEE Nucl Sci Symp Conf Rec; 1998. p. 1264-1267.
13. Siegel S, Vaquero JJ, Aloj L, Seidel J, Jagoda E, Gandler WR, Eckelman WC, Green MV. Initial results from a PET/planar small animal imaging system. IEEE Trans Nucl Sci Jun;1999 46(3): 571–575.
14. Lage E, Vaquero JJ, Sisniega A, Espana S, Tapias G, Abella M, Rodriguez-Ruano A, Ortuno JE, Udias A, Desco M. Design and performance evaluation of a coplanar multimodality scanner for rodent imaging. Phys Med Biol 2009:5427–5441. [PubMed: 19700817]

15. Murthy K, Aznar M, Bergman AM, Thompson CJ, Robar JL, Lisbona R, Loutfi A, Gagnon JH. Positron emission mammographic instrument: Initial results. Radiology 2000;215:280–285. [PubMed: 10751499]
16. Kao CM, Xie Q, Dong Y, Wan L, Chen CT. A high-sensitivity small-animal PET scanner: Development and initial performance measurements. IEEE Trans Nucl Sci Oct;2009 56(5):2678–2688.
17. Bao Q, Rannou FR, Taschereau R, Stout DB, Chatziioannou AF. Image reconstruction for PETbox, a benchtop preclinical PET tomograph. Proc IEEE Nucl Sci Symp Conf Rec 2009:2733–2737.
18. Bao Q, Zhang H, Douraghy A, Rannou FR, Chatziioannou AF. Design of a low cost benchtop preclinical PET system (PETbox) based on Monte Carlo simulations. Phys Med Biol. submitted for publication.
19. Chatziioannou AF, Tai YC, Doshi N, Cherry SR. Detector development for microPET II: A 1 micron resolution PET scanner for small animal imaging. Phys Med Biol 2001;46:2899–2910. [PubMed: 11720354]
20. Boellaard R, Buijs F, Jong HWAMd, Lenox M, Gremillion T, Lammertsma AA. Characterization of a single LSO crystal layer high resolution research tomograph. Phys Med Biol 2003;48:429–448. [PubMed: 12630740]
21. Rouze NC, Schmand M, Siegel S, Hutchins GD. Design of a small animal PET imaging system with 1 microliter volume resolution. IEEE Trans Nucl Sci Jun;2004 51(3):757–763.
22. Zhang N, Thompson CJ, Cayouette F, Jolly D, Kecani S. A prototype modular detector design for high resolution positron emission mammography imaging. IEEE Trans Nucl Sci Oct;2003 50(5): 1624–1629.
23. de Marcillac P, Coron N, Dambier G, Leblanc J, Moalic JP. Experimental detection of [alpha]-particles from the radioactive decay of natural bismuth. Nature 2003;422:876–878. [PubMed: 12712201]
24. Bao Q, Chatziioannou AF. GATE simulation of a BGO based high sensitivity small animal PET scanner. Proc Noninvasive Functional Source Imag Brain Heart Inter Conf Functional Biomed Imag 2007:47–50.
25. Goertzen AL, Suk JY, Thompson CJ. Imaging of weak-source distributions in LSO-based small-animal PET scanners. J Nucl Med 2007;48:1692–1698. [PubMed: 17873140]
26. Funk T, Sun M, Hasegawa BH. Radiation dose estimate in small animal SPECT and PET. Med Phys 2004;31:2680–2686. [PubMed: 15487751]
27. Taschereau R, Chatziioannou AF. Monte Carlo simulations of absorbed dose in a mouse phantom from 18-fluorine compounds. Med Phys 2007;34:1026–1036. [PubMed: 17441249]
28. Stickel JR, Qi J, Cherry SR. Fabrication and characterization of a 0.5-mm lutetium oxyorthosilicate detector array for high-resolution PET applications. J Nucl Med 2007;48:115–121. [PubMed: 17204707]
29. Siegel S, Silverman RW, Yiping S, Cherry SR. Simple charge division readouts for imaging scintillator arrays using a multi-channel PMT. IEEE Trans Nucl Sci Jun;1996 43(3):1634–1641.
30. Young JW, Moyers JC, Lenox M. FPGA based front-end electronics for a high resolution PET scanner. IEEE Trans Nucl Sci Aug;2000 47(4):1676–1680.
31. Laymon CM, Miyaoka RS, Park BK, Lewellen TK. Simplified FPGA-based data acquisition system for PET. IEEE Trans Nucl Sci Oct;2003 50(3):1483–1486.
32. Douraghy A, Rannou FR, Silverman RW, Chatziioannou AF. FPGA electronics for OPET: A dual-modality optical and positron emission tomograph. IEEE Trans Nucl Sci Oct;2008 55(5):2541–2545.
33. Guerra P, Sportelli G, Ortuo J, Ledesma-Carbayo MJ, Vaquero JJ, Desco M, Santos A. PETonCHIP: Architecture of a on-chip high-resolution, fully digital positron emission tomography scanner for small animal imaging. Proc IEEE Nucl Sci Symp Conf Rec 2007;5:3324–3327.
34. He B, Frey EC. Comparison of conventional, model-based quantitative planar, and quantitative SPECT image processing methods for organ activity estimation using in-111 agents. Phys Med Biol 2006;51:3967–3981. [PubMed: 16885618]

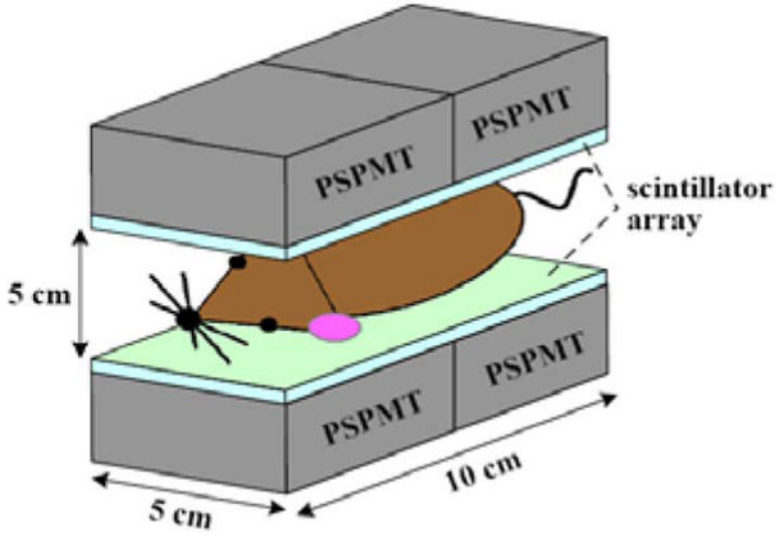

Fig. 1.

A conceptual drawing of the PETbox geometry. Two flat-panel type detectors, each having a sensitive area of approximately 5 cm × 10 cm, are placed opposing each other with a separation of 5 cm. Both the detectors and the mouse are kept stationary during the scan.

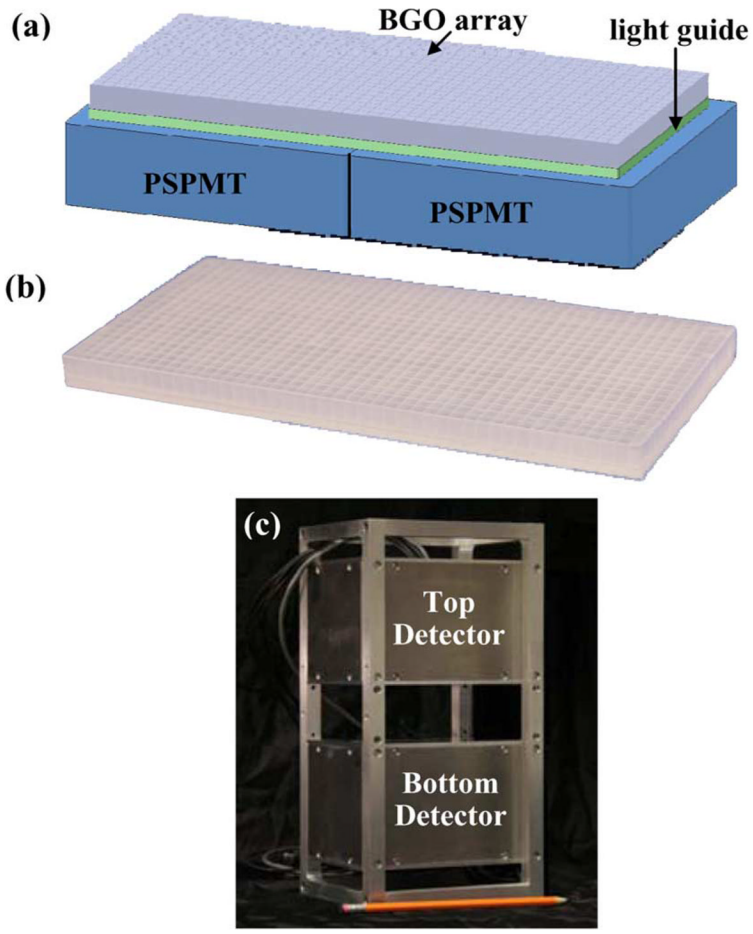

Fig. 2.

(a) Schematic drawing of the PETbox detector module. A light guide is inserted between the scintillator array and the PSPMTs to recover the dead space at the junction of the two tubes. (b) A 20 × 44 BGO array fabricated using the proposed method. (c) The finished gantry with two detector heads mounted.

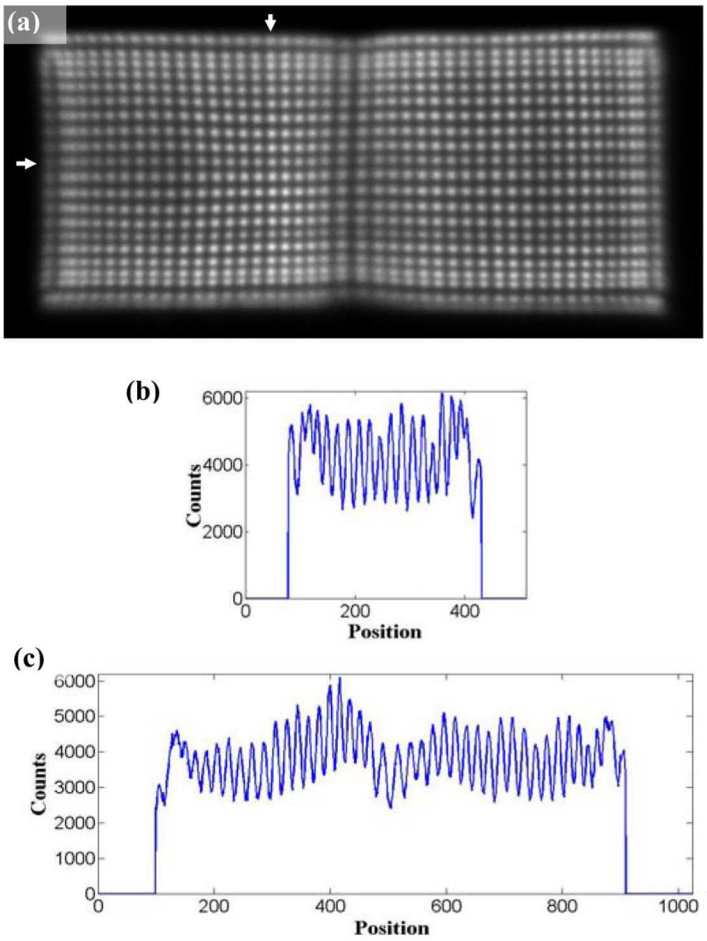

Fig. 3.

(a) Flood image taken from the top detector head. Profiles of counts along (b) 17th column and (c) 10th row of the flood histogram are also shown.

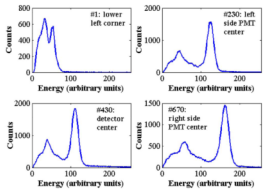

Fig. 4.

Energy spectra of four individual crystals on the top detector. FWHM energy resolutions are measured to be 38.5% for #1, 18.4% for #230, 18% for #430 and 16.5% for #670 respectively.

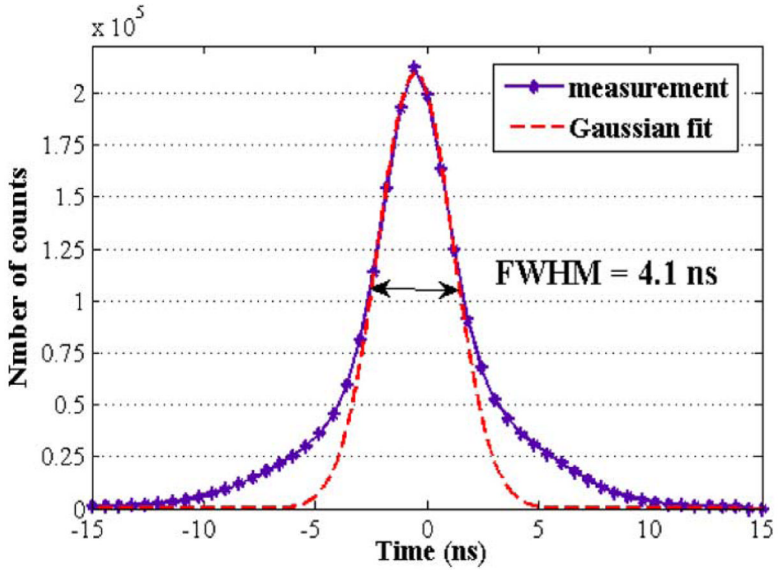

Fig. 5.
Measured coincidence timing distribution of the detector pair.

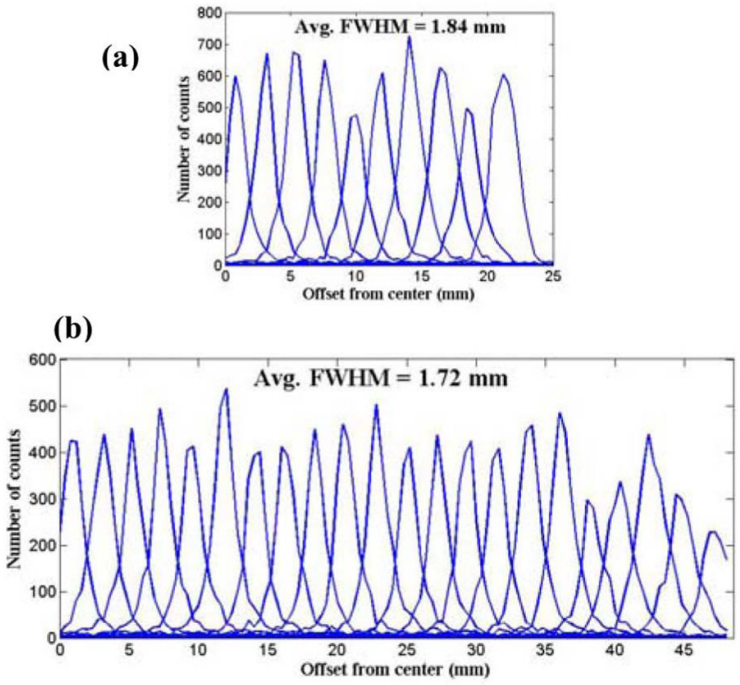

Fig. 6.

Intrinsic spatial resolution measured with a ^{22}Na point source stepping across the detector face from the center of FOV in the direction (a) along detector short axis and (b) along detector long axis.

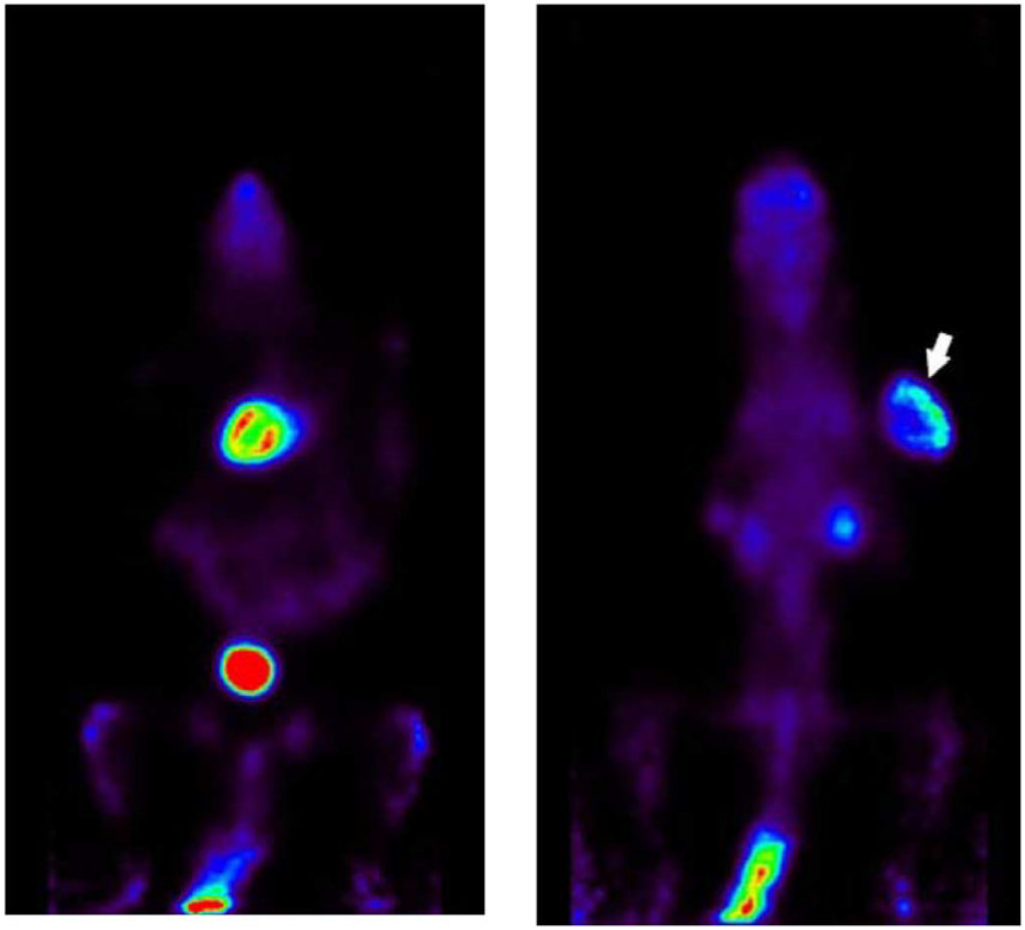

Fig. 7.

In-vivo scan of a mouse tumor xenograft performed following an 1 hour uptake with 32 μCi [^{18}F]FDG injected. The scan time was 20 minutes. Selected slices of the coronal section are displayed showing uptake in the heart and the tumor respectively.

TABLE I

Energy Resolution for the Two Detectors

	Top Detector			Bottom Detector		
FWHM	worst	best	mean	worst	best	mean
	38.5%	16.1%	20.1%	42.7%	15.5%	19.6%